Demonstration of Improving the Performance of a Fibre Optic Displacement Sensor Using the Optical Harmonic Vernier Effect by Cascading Tapered Optical Single-Mode Fibres

L. Guillen-Ruiz, G. Anzueto-Sanchez, A. Martínez-Rios, J. Camas-Anzueto, R. E. Nuñez-Gomez, and J. A. Martin-Vela

***Abstract*—An experimental demonstration for generating harmonics in the optical Vernier effect (OVE) by cascading tapered single-mode fibres (SMF28) is presented. The tapered optical fibres conformed to a pair of in-series Mach-Zehnder fibre interferometers (MZFI), in which one MZFI was a reference while the other was a sensor. The first-order harmonic was achieved by increasing the distance between tapers of the sensor MZFI by a multiple of (i + 1) times the distance between tapers of the reference MZFI plus a mismatch factor. A series of experiments using an individual MZFI and two MZFIs with traditional and harmonic OVE as displacement sensors were performed to compare their sensitivities and magnification factors and demonstrate the improving the sensitivity. The displacement sensor with the first-order harmonic exhibited a maximum sensitivity of −33.3 nm/mm with an M-factor of 8.53 in the mm range.**

***Index Terms*—Displacement sensor, free spectral range, harmonic, Mach-Zehnder, magnification, optical vernier effect, taper.**

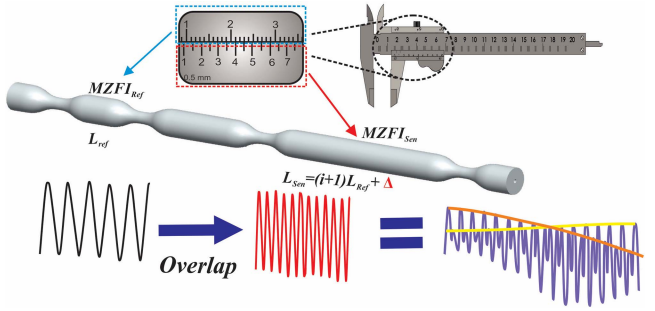

Fig. 1. Similar to a Vernier calliper with two different scales to achieve higher-resolution measurements, the OVE uses the superposition response of two interferometers with slightly different frequencies. The innovative concept of the optical harmonic Vernier effect facilitates using two interferometers with very different frequencies to create a complex harmonic response with improved resolution and detection capabilities compared to the traditional OVE.

I. Introduction

THE optical Vernier effect (OVE) is a tool that improves the sensitivity and resolution of interferometry-based optical fibre optic sensors. Two interferometric signals with slightly detuned frequencies are used [1], [2], which may sometimes be challenging because both interferometers must have similar sizes, which reduces some design possibilities. Harmonic generation in the OVE is a recent concept that addresses this difficulty because only one of the interferometers' optical path length (OPL) must be increased.

The OPL increase is expressed in multiples of i (where i is an integer) to the second interferometer plus a detuning factor, as shown in Fig. 1, where $MZFI_{Ref}$ and $MZFI_{Sen}$ are the Mach-Zehnder fibre interferometers (MZFI) reference and sensor, respectively. L_{Ref} and L_{Sen} denote the separation between tapers for the first and second interferometers, respectively.

The concept of the optical harmonic Vernier effect has been present since 2015 in pressure sensors [3], [4], hydrogen sensors [5], strain sensors [6], DNA hybridisation sensors [7], and salinity sensors [8]. However, the concept was not utilized to improve sensors at that time.

The chronologically ordered text shows how the authors achieved the optical harmonic Vernier effect using different types of interferometers. Gomes et al. [9] presented an extended concept of an optical harmonic Vernier effect (OHVE) for the first time for Fabry-Perot interferometers (FPI). Robalinho et al. [10] showed the first-order harmonic to demonstrate a strain sensor. The first harmonic appears when the length of the first fibre-loop mirror (internal elliptical cladding) is approximately twice that of the second fibre-loop mirror (e-core section). Gomes et al. [11] developed a strain-sensing structure consisting of two FPI connected in series (both are sensing interferometers). Harmonics result from increasing the OPL of one of two interferometers by multiple times the OPL of the other one. In addition, the same author [12] proposed a few-mode fibre-optic

Manuscript received 7 June 2023; revised 25 July 2023; accepted 3 August 2023. Date of publication 7 August 2023; date of current version 21 August 2023. This work was supported by Conahtcyt. *(Corresponding author: G. Anzueto-Sanchez.)*

L. Guillen-Ruiz and J. Camas-Anzueto are with the Departamento de Posgrado e Investigación, Instituto Tecnológico de Tuxtla Gutierrez, Tuxtla Gutierrez, Chiapas 29050, México.

G. Anzueto-Sanchez and A. Martínez-Rios are with the Centro de Investigaciones en Óptica, León 37105, México (e-mail: gilberto.anzueto@gmail.com).

R. E. Nuñez-Gomez is with the Instituto Tecnológico de Zacatepec, Zacatepec, Morelos 62780, México.

J. A. Martin-Vela is with the Instituto Tecnológico de Conkal, Conkal, Yucatán 97345, México.

Digital Object Identifier 10.1109/JPHOT.2023.3303083

This work is licensed under a Creative Commons Attribution 4.0 License. For more information, see https://creativecommons.org/licenses/by/4.0/

FPI in combination with an FPI reference. The harmonic occurs when the reference interferometer's length is twice the sensing interferometer's length.

Subsequently, Robalinho et al. [13] proposed a sensor with nano-displacement capability. The first and second harmonic orders appear when the sensor cavity lengths are approximately double and triple the reference cavity length, respectively. Yang et al. [14] demonstrated the harmonics in a pressure sensor using two FPI connected in cascade and fabricated using silica hollow fibre cavities. They obtained the harmonics through the ratio of the lengths between the reference and sensor FPIs. Wang et al. [15] reported an adjustable FPI piezometer based on a parallel structure for water level measurements. The harmonics were obtained by manually adjusting the cavity length of the piezometer. Liu et al. [16] proposed a temperature sensor with cascaded Sagnac loops based on a polarisation-maintaining fibre and obtained harmonics when the length of one Sagnac loop fibre was an integral multiple of the length of the other Sagnac loop. Zhu et al. [17] developed a humidity sensor with a pair of FPI connected in a cascade and chitosan film. They obtained the harmonic by manipulating the thickness of the chitosan film and the cavity distance between the SMF and chitosan film. Lou et al. [18] demonstrated a gas-pressure sensor with a pair of FPIs in a parallel configuration. The harmonic appears when the length of the capillary tube of the FPI reference is approximately i + 1 times the length of the capillary tube of the FPI sensor. Yang et al. [19] fabricated a gas pressure sensor with a parallel-connected FPI based on hollow-core Bragg fibres (HCBF) and hollow silica tubes (HST). They achieved a first-order harmonic by increasing the OPL of the first FPI by i + 1 times the OPL of the second FPI by modifying the refractive index (RI) and cavity length. Finally, Chen et al. [20] presented an open cavity Fabry-Perot interferometer (OCFPI) encapsulated with polydimethylsiloxane (PDMS) for temperature measurements. The fourth-order harmonic was obtained by increasing the OPL of the sensor interferometer (open cavity) multiple i times the reference interferometer (silica cavity).

In contrast to the related literature, this article demonstrates the generation of the first harmonic by concatenating two MZFIs based on tapered single-mode fibre optic (SMF28) sections under certain conditions. The harmonic appears when the OPL of the sensor interferometer increases by a multiple (i + 1 times) of the OPL of the reference interferometer plus a mismatch factor. The novelty in generating harmonics is that it allows the difference in frequencies between the two MZFIs to be vastly and easily manipulated compared to the slight difference in frequencies between the two MZFIs of the OVE.

II. Theoretical Background and Experimental Setup for the Generation of the Harmonic Optical Vernier Effect

Harmonic OVE occurs when the OPL of the first interferometer increases by (i + 1) times that of the second interferometer plus a mismatch factor Δ (Fig. 2). According to [9], this is expressed as

$$OPL_{sen} = (i+1)\,OPL_{ref} + \Delta \tag{1}$$

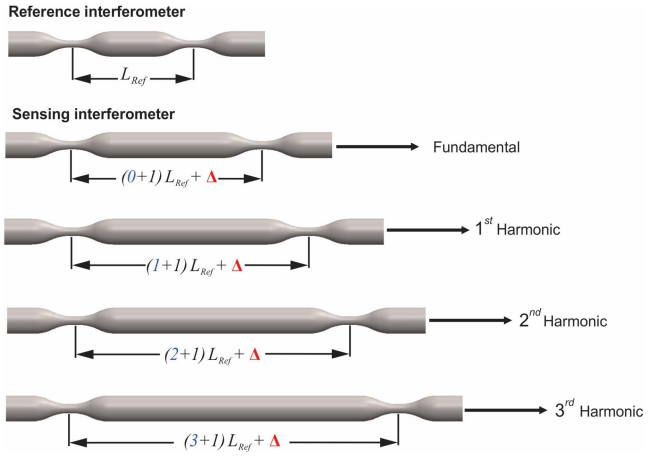

Fig. 2. Dimensions of the concatenated optical SMFs to obtain OVE and the first three harmonic orders.

where "i" is a positive integer that denotes the order of the harmonics and Δ is a mismatch factor deliberately applied to $\mathrm{OPL_{Sen}}$ to move away slightly from the exact value of "i + 1" $\mathrm{OPL_{Ref}}$. $\mathrm{OPL_{Sen}}$ and $\mathrm{OPL_{Ref}}$ are the lengths of the optical paths of the sensor and reference, respectively.

From (1), the OPL is related to the length between tapers, as follows:

$$L_{sen} = (i+1)\,L_{ref} + \Delta \tag{2}$$

Two envelope types appear in the harmonic spectrum, one external and the other internal. Gomes et al. [9] reported that the FSR of the outer envelope is a function of the FSR of both interferometers (sensor and reference) and resembles the FSR of the envelope of a traditional OVE. Therefore, the harmonic OVE regenerates the external envelope with the same frequency and FSR as the conventional OVE. $FSR^{i}_{External}$ is obtained using the following equation:

$$FSR^{i}_{External} = \frac{FSR_{Ref}FSR^{i}_{sen}}{|FSR_{Ref} - (i+1)\,FSR^{i}_{sen}|} \tag{3}$$

where $\mathrm{FSR_{Ref}}$ and $\mathrm{FSR^{i}_{Sen}}$ are the FSRs of the reference and sensor interferometers for the i-th order harmonic.

According to Gomes [22], using the external envelope for sensing applications and measuring the change in wavelength has a significant drawback because the visibility of the exterior envelope decreases as the harmonic order increases. Zhao et al. [23] indicated that increasing the ratio of the OPL by integer multiples maintains the length mismatch factor and reduces the visibility of the external envelope while keeping its FSR constant. An alternative technique that involves the use of inner envelopes is used to solve this problem. The intersections between the inner envelopes provide multiple points that can be used to track changes in wavelength. According to the order i of the harmonics, the inner envelopes increase proportionally to the number and range of the FSR, which makes it easy to track spectral changes by monitoring the intersections produced by the envelopes.

Another advantage of using inner envelopes is that the effects of intensity fluctuations in the different peaks are reduced, and the FSR and frequency (inverse of the FSR) of the internal envelope increase with the order of the harmonics. The FSR of the internal envelope is defined as

$$FSR_{Int} = \frac{(i+1)\,FSR_{Ref}FSR^{i}_{sen}}{|FSR_{Ref} - (i+1)\,FSR^{i}_{sen}|} = (i+1)\,FSR^{i}_{Upper} \quad (4)$$

where FSR^{i}_{Upper} is the FSR of the external envelope, similar to the envelope of the traditional OVE. According to [7], the M factor can be defined in two ways. The first relates the $FSR_{Envelope}$ and FSR_{Sen} and indicates how large the FSR of the envelope is compared to the FSR of the MZFI sensor, as shown below:

$$M_{Int} = \frac{FSR_{Int}}{FSR_{Sen}} = \frac{\frac{(i+1)FSR_{Ref}FSR^{i}_{sen}}{|FSR_{Ref}-(i+1)FSR^{i}_{sen}|}}{FSR_{Sen}} = \left|\frac{(i+1)\,FSR_{Ref}}{FSR_{Ref} - (i+1)\,FSR^{i}_{sen}}\right| = (i+1)\;M \quad (5)$$

The second definition of the M-factor is directly related to sensor detection. It describes the magnification of the wavelength shift of the envelope compared with an individual MZFI sensor. Therefore, the sensitivity of the harmonic OVE for the i-th order is compared with respect to the sensitivity of an individual MZFI and is expressed as follows:

$$M = \frac{S^{i}_{Envelope}}{S_{sen}} \quad (6)$$

In an MZFI, (2) is used to obtain the distance between the tapers of the MZFI sensor. The OVE is obtained when i = 0 and a mismatch factor Δ is added ($L_{Sen} = (0+1)L_{Ref} + \Delta$). The first harmonic order is obtained with i = 1, by doubling the length of the reference MZFI and adding the length mismatch factor ($L_{Sen} = (1+1)L_{Ref} + \Delta$)).

To obtain external envelopes with greater precision in the traditional OVE, we used the Hilbert-Huang algorithm [24], [25], [26], and for the internal envelopes, we used the fitting algorithm proposed by Gomes et al. [9]. The instantaneous amplitude of the analytical signal was used to obtain the envelopes of the signals. The Hilbert-Huang transform enhanced only the form of the external envelope.

Fig. 3 shows the experimental setup for obtaining the first-order harmonic by cascading tapered optical single-mode fibres. The broadband fluorescent light source (1500-1600 nm) consists of a 3 m-long erbium-doped fibre (EDF, LIEKKI Er 16-8/125) pumped through a wavelength divider multiplexer (WD202A from Thorlabs) with a 976-nm laser diode (BL976-SAG300, Thorlabs). The concatenated tapers are spliced after the EDF super-fluorescent source. The resolution of the optical spectrum analyzer (OSA) was 0.05 nm for each measurement.

All interferometers were fabricated on a standard SMF-28 using a GPX 3400 Vytran glass processing system. The geometrical dimensions of the tapered sections included a transition length (TL) of 3 mm, waist length (WL) of 1 mm, and waist diameter (WD) of 60 μm. The processor system guarantees very high-quality profiles and reproducibility of the tapers. We use a routine (fusion power of 42 W and pull velocity of 1.5 mm/s) to ensure high precision in controlling the taper WD and TL.

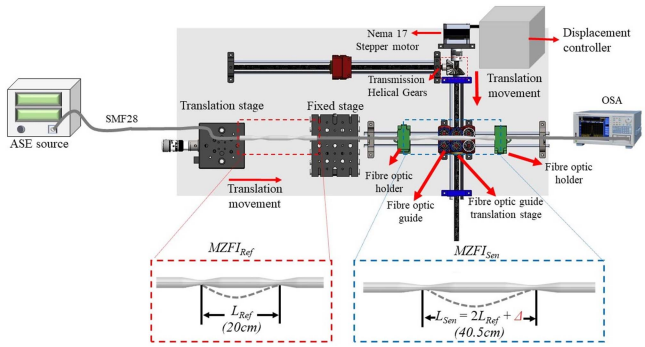

Fig. 3. Schematic diagram of the experimental setup for displacement measurement with an in-cascade MZFI tapered optical fibre structure used to obtain harmonic OVE.

TABLE I
MAIN PARAMETERS OF THE EXPERIMENTS

Method	L_{Ref} (cm)	L_{Sen} (cm)	FSR_{Ref} (nm)	FSR_{Sen} (nm)	FSR_{Env} (nm)	M-Factor	Order (M_H/M_F)
Experimental setup 1							
Tradicional	39	44	1.09	0.99	11.84	12.12	1.99 **(2)**
1st Harmonic	39	77.5	1.09	0.59	33.07	24.22	
Experimental setup 2							
Tradicional	25	30	1.75	1.47	9.18	6.25	2.07 **(2)**
1st Harmonic	25	49.5	1.75	0.74	38.28	12.96	
Experimental setup 3							
Tradicional	20	25	2.30	1.74	7.14	4.10	2.07 **(2)**
1st Harmonic	20	40.5	2.30	1.01	45.06	8.51	

The working principle of the experimental setup was described in a previous study [21]. In this proposal, the displacement process was automated. A controller was programmed to enable the stepper motor to produce a displacement of 0.05 mm. The stepper motor transmitted the displacement through the lead screw to the fibre-optic translation stage (See Fig. 3).

When both MZFIs are in a straight position, no interference pattern occurs because there is no excitation of higher-order cladding modes. Afterward, the $MZFI_{Ref}$ is gradually bent to generate the comb-filtering characteristic until a high-contrast interference pattern is obtained [21]. Then, $MZFI_{Sen}$ is bent until the OVE pattern appears. Finally, the displacement measurement begins when the OVE pattern occurs in the displacement values given in the experimental results section.

Three experiments were analysed using the summarised parameters in Table I.

III. EXPERIMENTAL RESULTS

Figs. 4, 5, and 6 track the intersection of the internal envelopes of the first-order harmonic (indicated by the red dotted circle) as a function of three linear shifts. In Fig. 4 the results from the first experiment are shown. The internal envelope intersection occurs at approximately 1558 nm when the displacement is 1.5 mm (Fig. 4(b)). As the displacement increases to 2.25 mm (Fig. 4(d)) and 3 mm (Fig. 4(f)), the internal envelope intersection shifts to shorter wavelengths.

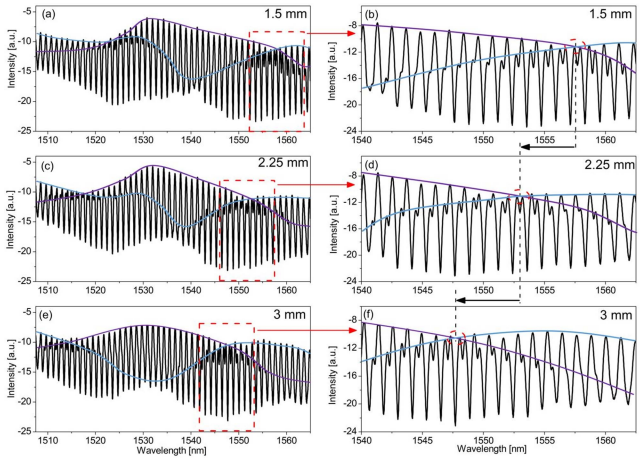

Fig. 4. Experimental wavelength shift of the harmonic spectrum for three displacement values: (a), (b) 1.5 mm and its magnified image, (c), (d) 2.25 mm and its magnified image, (e), (f) 3 mm and its magnified image. A dotted red circle indicates one of the two intersections. As the displacement is applied, the wavelength shift of the internal envelopes towards shorter wavelengths is clearly visible compared to the OVE.

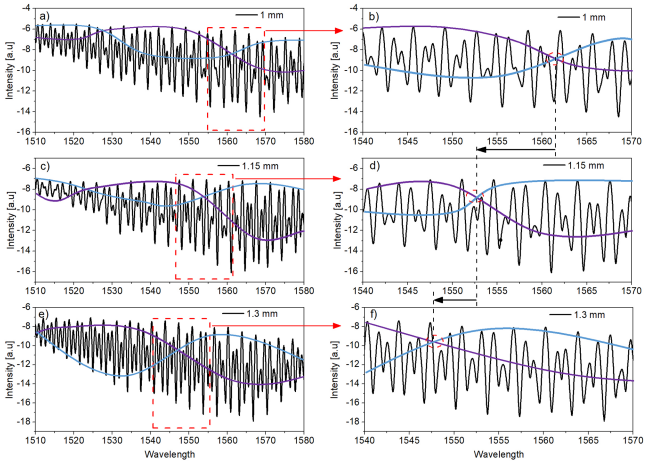

Fig. 5. Depicts the experimental wavelength shift of the harmonic spectrum for three displacement values: (a), (b) 1 mm and its magnified image,); (c), (d) 1.15 mm and its magnified image; (e), (f) 1.3 mm and its magnified image. A dotted red circle indicates one of the two intersections. As the displacement is applied, the wavelength shift of the inner envelopes towards shorter wavelengths is clearly visible compared to the OVE.

Fig. 5 corresponds to the results from the second experiment. The internal envelope intersection occurs around 1560.94 nm when the displacement is 1 mm (Fig. 5(b)). As the displacement increases to 1.15 mm (Fig. 5(d)) and 1.3 mm (Fig. 5(f)), the internal envelope intersection shifts to shorter wavelength positions.

Fig. 6 illustrates the results from the third experiment. When the displacement is 1.8 mm, there is only one intersection observed at approximately 1532.5 nm (Fig. 6(b)). As the displacement increases by 1.95 mm (Fig. 6(d)) and 2.1 mm (Fig. 6(f)), the internal envelope intersection shifts to shorter wavelengths.

Fig. 7 compares the FSR of the envelope of the OVE with the FSR of the internal envelopes of the first-order harmonic. Similar to the first experimental setup, the signals of the reference and

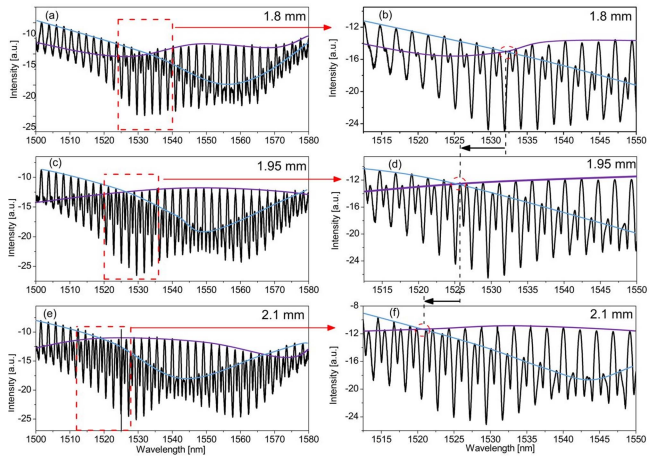

Fig. 6. Display the experimental wavelength shift of the harmonic spectrum for three displacement values: (a), (b) 1.8 mm and its magnified image; (c), (d) 1.95 mm and its magnified image; (e), (f) 2.1 mm and its magnified image. A dotted red circle indicates one of the two intersections. As the displacement is applied, the wavelength shift of the inner envelopes towards shorter wavelengths is clearly visible compared to the OVE.

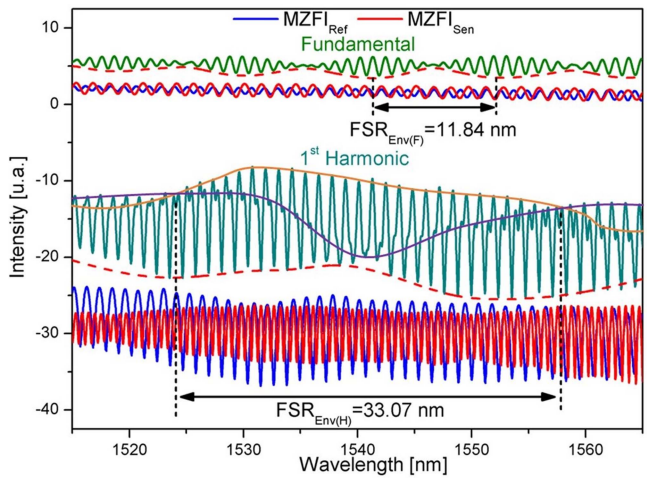

Fig. 7. Depicts a comparison of the increase in FSR between the OVE and first-order harmonic first experiment specifically for two different distances: (39–44 cm and 39–77.5 cm).

sensor interferometers must be in phase for the envelope to occur. In the traditional case, the envelope occurs every 11.84 nm, while in the first-order harmonic, it occurs every 33.07 nm.

Fig. 8 compares the FSR of the envelope of the traditional OVE with the FSR of the internal envelopes of the first harmonic OVE. In the second experimental setup, the envelope occurred when the reference interferometers and sensor signals were in phase. In the traditional case, this occurred every 9.18 nm, while in the first-order harmonic OVE occurred every 38.28 nm.

Fig. 9 illustrates a comparison between the FSRs of the traditional OVE envelopes and the first-order harmonic's internal envelope. To observe the envelopes, the signals from the reference and sensor interferometers need to be in phase. In the third experiment, the envelope occurs every 7.14 nm in the traditional OVE, while in the first-order harmonic, it occurs every 45.06 nm.

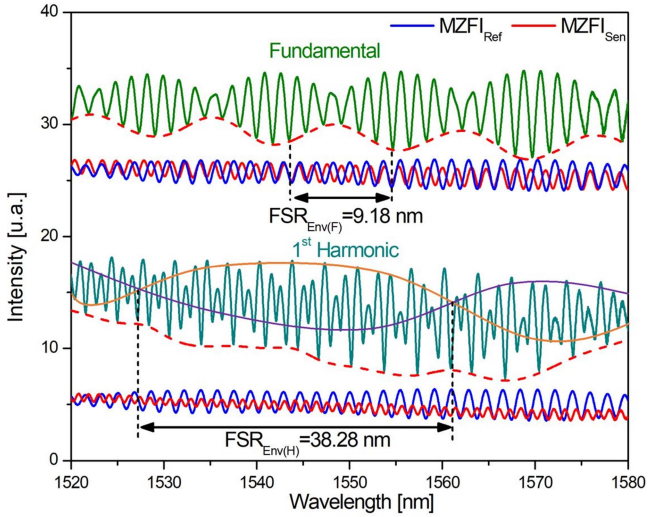

Fig. 8. Comparison of the increase in FSRs of the OVE and first-order harmonic of the second experiment (25–30 cm and 25–49.5 cm).

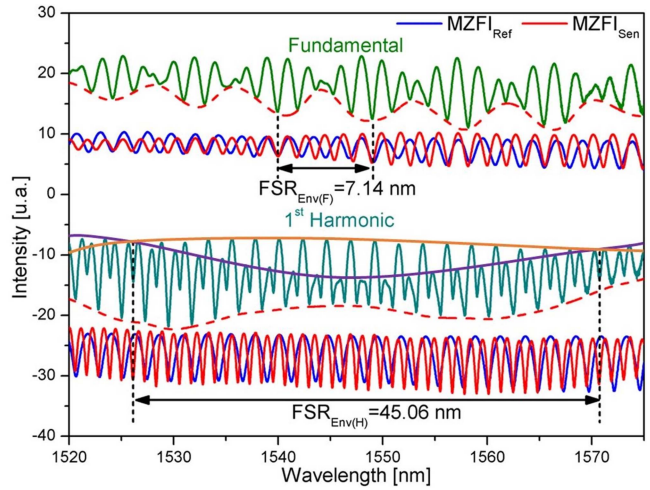

Fig. 9. Comparison of the increase in FSRs of the third experiment (20–25 cm and 20–40.5 cm).

Fig. 10 presents the frequency analysis with measurements from the third experiment, where $L_{Ref} = 20$ cm and $L_{Sen} = 40.5$ cm. Fig. 11(a) and (c) show the transmission spectra of $MZFI_{Ref}$ and $MZFI_{Sen}$, respectively, while (c) shows the superimposed spectra. Fig. 10(b), (d), and (f) show their spatial frequencies. The prominent peaks in Fig. 10(b) and (d) indicate the dominant frequencies of $MZFI_{Ref}$ and $MZFI_{Sen}$, which are 0.4347 nm^{-1} and 0.9900 nm^{-1}, respectively. These frequencies are reflected in Fig. 10(f) in the adjacent peaks of the same frequency, whereas the frequency of the superimposed spectrum is reflected in the first peak that appears in Fig. 10(f) at 0.0221 nm^{-1}.

First, we examined the spectral response resulting from the displacement of a single MZFI sensor with a distance of 44 cm between tapers. Subsequently, we analysed the spectral response of a traditional OVE. Finally, the spectral response of a first-order harmonic OVE was analysed with the same linear displacement, as shown in Fig. 11. For all devices, a linear displacement

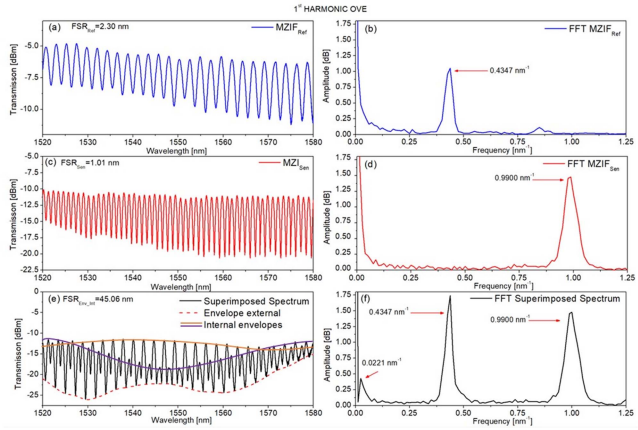

Fig. 10. (a) and (c) show the transmission spectra of $MZFI_{Ref}$ and $MZFI_{Sen}$, respectively; (b) and (d) correspond to the FFT of the two MZFIs; (e) is the overlapped transmission spectrum of the two MZFIs; and (f) is the FFT of the overlapped spectrum.

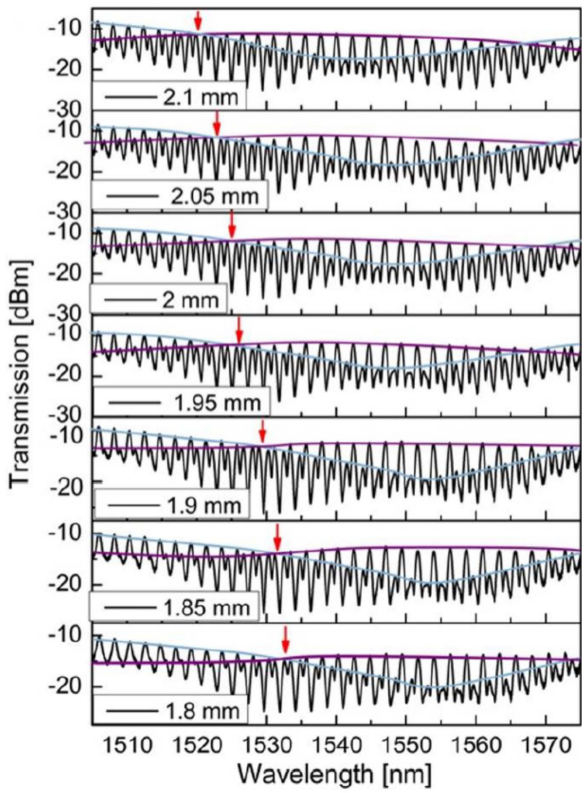

Fig. 11. Spectral shift of the envelope for different displacement values for the first-order harmonic.

was gradually applied from 1.8 mm to 2.1 mm at intervals of 0.05 mm.

The sensitivity of the OVE was determined to be −3.03 nm/mm, magnified 12.12 times compared to the sensitivity of the single MZFI sensor (−0.2485 nm/mm). On the other hand, the sensitivity of the first-order harmonic was found to be −5.99 nm/mm, magnified 24.22 times compared with respect to a single MZFI sensor.

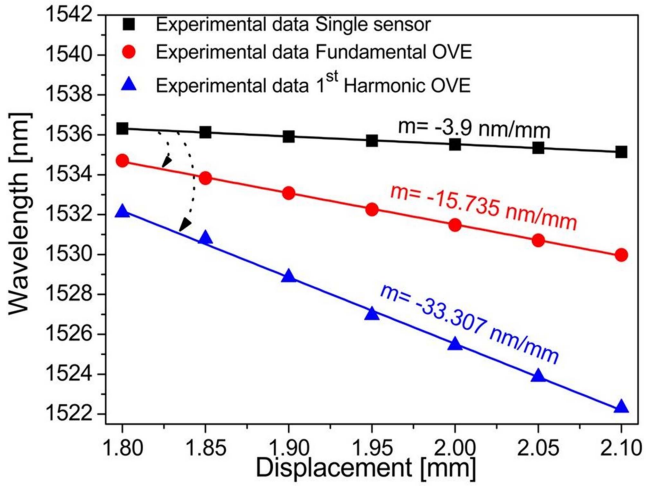

Fig. 12. Linear adjustment results of the linear displacement measurement sensitivity of an individual MZFI (black), traditional OVE (red), and first harmonic of the OVE (blue).

This result highlights that the internal envelope of the harmonic shifts considerably more than the external envelope of the OVE. These findings are illustrated in Fig. 12.

Later, we examined the spectral response resulting from the displacement of a single MZFI sensor with a distance of 30 cm between the tapers. Subsequently, we analyzed the spectral response of a traditional OVE. Finally, we analyzed the spectral response of a first-order harmonic OVE, which is shown in Fig. 13. For all devices, a linear displacement was applied gradually, ranging from 1 mm to 1.3 mm at intervals of 0.05 mm.

Fig. 14 shows the sensitivity of the three analysed structures: simple MZFI (black), traditional OVE (blue), and first-order harmonic OVE (red). The sensitivity of the OVE was −13.8642 nm/mm, which was magnified 6.25 times compared to that of the single MZFI sensor (−2.1071 nm/mm). The sensitivity of the first-order harmonic was −27.6214 nm/mm, magnified 12.96 times compared with respect to a single MZFI sensor.

Finally, we examined the spectral response resulting from the displacement of a single MZFI sensor with a distance of 44 cm between the tapers. Subsequently, we analyzed the spectral response of a traditional OVE. Finally, we analyzed the spectral response of a first-order harmonic OVE, which is shown in Fig. 15. For all devices, we applied linear displacement gradually, ranging from 1.5 mm to 3 mm at intervals of 0.25 mm

Fig. 16 shows the sensitivity of the three analysed structures the simple MZFI (black), the traditional OVE (blue), and the first-order harmonic OVE (red). The sensitivity of the OVE was −15.735 nm/mm, magnified 4.10 times compared to that of the single MZFI sensor (−3.9 nm/mm). The sensitivity of the first-order harmonic was −33.307 nm/mm, magnified 8.53 times compared with respect to a single MZFI sensor.

IV. Discussion

One advantage of the harmonics over the traditional OVE is that the spectral tracking for harmonics is relatively easy to perform. Conversely, the conventional OVE requires data processing techniques like applying the Hilbert-Huang transform or the Gauss-fitting algorithm that highly depends on the number of considered points to accurately track the position and the aspect of the envelopes [22].

On the other hand, Table II compares the performance of the devices, namely single MZFI, traditional and first harmonic. The second column corresponds to the sensitivities and shows a

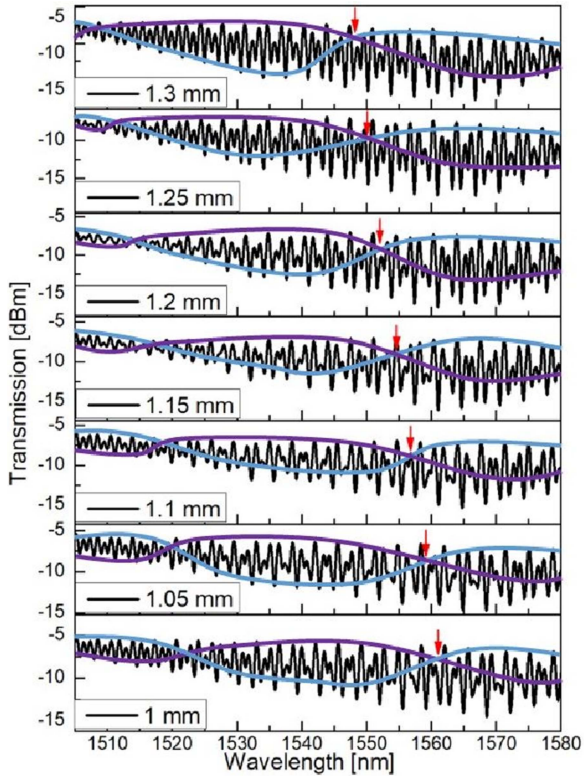

Fig. 13. Change in the position of the first-order envelope for different displacement values.

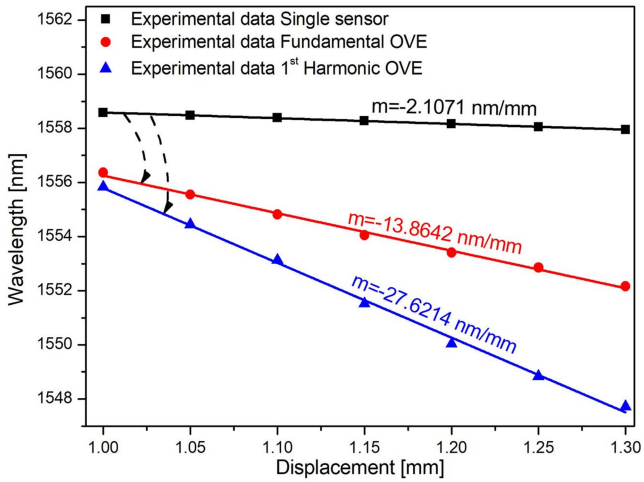

Fig. 14. Linear adjustment results of the linear displacement measurement sensitivity of an individual MZFI (black), traditional OVE (red), and first harmonic of the OVE (blue).

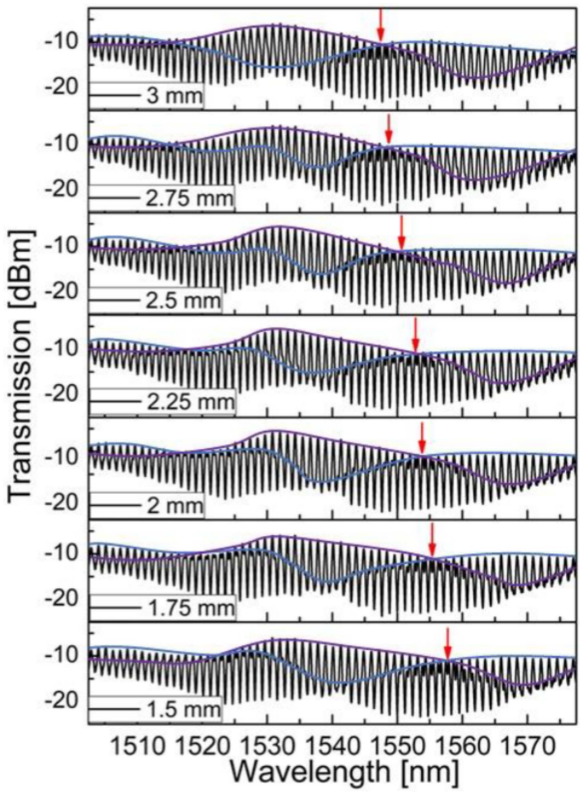

Fig. 15. Change in the position of the first-order envelope for different displacement values.

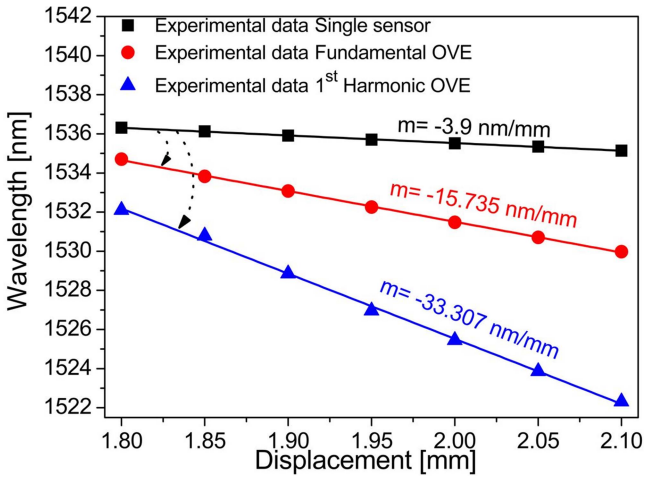

Fig. 16. Linear adjustment results of the linear displacement measurement sensitivity of an individual MZFI (black), traditional OVE (red), and first harmonic of the OVE (blue).

significant improvement for the first-order harmonic compared to the traditional OVE and the MZFI. The third column shows the length of the MZFI sensor. Upon comparing the lengths of the MZFI sensors of each device (single with single, traditional with traditional, and 1st harmonic with 1st harmonic), we discovered an inversely proportional between the lengths of the MZFI sensors to the sensitivities. At the same time, they were directly proportional to the M-factor. The fourth column

TABLE II
PERFORMANCE COMPARISON OF THE MEASUREMENT DEVICES

Method	Sensitivity (nm/ mm)	L_{Sen} (cm)	Range (mm)	M-factor By FSR (Eq. 5)	M-factor By Sensitivity (Eq. 6)	M_{int}= (i+1) M i=1 (Eq. 5)
Experimental setup 1						
Single MZFI	-0.2485	44	1.5-3 (1.5)	-	1	(2) (12.12) = **24.24**
Traditional	-3.03	44		12.12	12.18	
1st Harmonic	-5.99	77.5		**24.22**	**24.09**	
Experimental setup 2						
Single MZFI	-2.1071	30	1-1.3 (0.3)	-	1	(2)(6.25)= **12.5**
Traditional	-13.8642	30		6.25	6.57	
1st Harmonic	-27.6214	49.5		**12.96**	**13.10**	
Experimental setup 3						
Single MZFI	-3.9	25	1.8-2.1 (0.3)	-	1	(2) (4.10) = **8.20**
Traditional	-15.735	25		4.10	4.03	
1st Harmonic	-33.307	40.5		**8.51**	**8.53**	

indicates the range of each device. The fifth and sixth columns show the values of the M-factor calculated using (5) and (6). Notably, the M-factor of the first-order envelope is twice that of the OVE, coinciding with the order calculated in Table I. The last column shows the M-factor of the inner envelope of the first-order harmonic.

Table III summarises the works that demonstrated harmonics for different sensor applications. The table is chronologically ordered, showing the year, the configuration, i.e., type of interferometer, sensing parameter, measurement range, maximum order of the harmonics, type of device, sensitivity, and M-factor.

The tool of using the harmonics of the OVE is a technique that has been discovered relatively recently (in 2019 ref. [9]) and exhibits the capability to improve the sensitivity of sensors because sensitivity increased considerably with the order of the harmonics compared to a sensor exhibiting OVE or an individual sensor [10], [11], [12], [13], [14], [16], [17], and [19] in a same measurement range. In other cases [9], [15], and [18], using the third-order harmonic was ineffective because the increase in sensitivity was limited to the available wavelength span in the detection system.

The OVE significantly increases the sensitivity of a sensor by increasing its OPL. In a previous study, we experimentally showed that the distance between tapers is directly proportional to the OPL and inversely proportional to the free spectral range (FSR) [21]. However, the inherent drawback that the OPL of both MZFIs must be very similar in size complicates the design of possible sensors. In contrast, the concept of the harmonics increases the design options because only the distance between the tapers of the interferometer sensor and the distance between the tapers of the interferometer reference must be modified.

On the other hand, in the Fabry-Perot interferometers or relatively complex structures, the short lengths of these interferometers (of the order of micrometres) make it easier to achieve a harmonic of order greater than two. ([9], [12], [13], [15], [17], [18], [20]). However, sophisticated equipment and techniques must be used because the distances required to obtain the harmonics are of the order of micrometres or less, which in some cases may be challenging to manufacture.

Sensors that use (2) and have long lengths (of the order of meters) exhibit good sensitivity and a large M-factor. However, second or higher orders are challenging to obtain because the final length of the sensor would be impractical to manipulate if an

TABLE III
COMPARISON OF DIFFERENT MEASUREMENT DEVICES THAT EXHIBIT HARMONICS

Year	Configuration	Application	Measurement Range	Order Max.	Test	Sensitivity	M Factor	Ref.
2019	Fabry-Perot in parallel with capillary tube	Strain	0-100 με	3	Single i=1 i=2 i=3	3.37 pm/με 27.6 pm/με 93.4 pm/με 59.6 pm/με	1 8.18 27.7 17.7	[9]
2020	Two-fibre loops mirrors in series	Strain	0-800 με	1	Single Fund. i=1	15.46 pm/με 80 pm/με 120 pm/με	1 5 8	[10]
2020	Fabry-Perot with hollow capillary tube	Strain	0-500 με	1	Single Fund. i=1	1.07 pm/με 65.3 pm/με 146.3 pm/με	1 61 136.7	[11]
2020	Fabry-Perot in parallel with two access holes milled in the sensing FPI	RIU	0-8x10^{-5} RIU	1	Single i_{SM}=1 i_{TM}=1	-568 nm/RIU -28,496 nm/RIU -41,8387 nm/RIU	1 50.2 865	[12]
2021	New optical fibre structure consisting of a cleaved fibre and drop-shaped microstructure	Displacement	0-1000 nm	2	Single Fund. i=1 i=2	1.05 nm/μm 15.1 nm/μm 24.7 nm/μm 28.3 nm/μm	1 14 24 27	[13]
2021	FPI in cascade with two hollow silica capillaries	Gas Pressure	1-101 kPa	1	Single Fund.$_1$ Fund.$_2$ Fund.$_3$ i=1	- -31.8 pm/kPa -37.6 pm/kPa -55.7 pm/kPa -80.8 pm/kPa	- 7.36 8.7 12.9 18.7	[14]
2021	In-situ adjustable fibre-optic piezometer based on parallel structure external FPI	Water level	0-20 cm	3	Single$_1$ Fund.$_1$ i_1=1 i_1=2 i_1=3	-0.1475 nm/cm -7.0162 nm/cm -4.381 nm/cm -9.0817 nm/cm -2.5172 nm/cm	1 47.57 29.7 61.57 17.07	[15]
					Single$_2$ Fund.$_2$ i_2=1 i_2=2 i_2=3	-0.3075 nm/cm -7.2208 nm/cm -7.4466 nm/cm -4.1962 nm/cm -1.3774 nm/cm	1 23.48 24.22 13.65 4.48	
2021	Two cascading two Sagnac loops with polarisation maintaining fibre	Temperature	30-70 °C	1	Single Fund. i=1	-0.163 nm/°C -2.12 nm/°C -3.66 nm/°C	1 1.7 22.5	[16]
2022	A chitosan film cascaded FPI	Relative humidity	46-60 %	16	Fund. i=4. i=16	-1.57 nm/% RH -52.26 nm/% RH -83.77 nm/% RH	1 33.28 53.98	[17]
2022	FPIs connected in parallel with two segments of hollow-core capillaries	Gas Pressure	10-189 KPa	3	Single$_1$ Fund.$_1$ i_1=1 i_1=2 i_1=3	4.2 pm/KPa - 86.55 pm/KPa 279.52 pm/KPa 148.75 pm/KPa	1 - 20.6 66.6 35.4	[18]
					Single$_2$ Fund.$_2$ i_2=1 i_2=2 i_2=3	-4.2 pm/KPa - -74.6 pm/KPa -105 pm/KPa -159 pm/KPa	1 - 17.8 24.3 34.7	
2022	FPIs connected in parallel based on HCBF with HST	Gas Pressure	0-0.5 MPa	1	Single Fund. i_1	4.08 nm/MPa - 119.3 nm/MPa	1 - 29.24	[19]
2022	OCFPI encapsulated with the PDMS film	Temperature	40-60 °C	4	Single Fund. i_4	-10 pm/°C -0.32 nm/°C -3.4 nm/°C	1 - 11	[20]
2023	In-cascade MZFs concatenated tapered optical fibres	Displacement	1.5-3 mm	1	Single$_1$ Fund.$_1$ i_1=1	-0.2485 nm/mm -3.03 nm/mm -5.99 nm/mm	1 12.18 24.09	This Work
			1-1.3 mm		Single$_2$ Fund.$_2$ i_2=1	-2.107 nm/mm -13.8642 nm/mm -27.6214 nm/mm	1 6.57 13.10	
			1.8-2.1 mm		Single$_3$ Fund.$_3$ i_3=1	-3.9 nm/mm -15.735 nm/mm -33.307 nm/mm	1 4.03 8.53	

improvement through the second or third order of the harmonic is sought ([10], [16]).

Sensors whose OPL depends on the dimensions of the interferometers and refractive index ([11], [14], and [19]) use (1). In these sensors, the length of one of the interferometers is a function of the size of the cavity of another interferometer, and the length mismatch factor Δ depends on the refractive index of the interferometers. The dimensions of this class of sensors cannot be directly obtained through increased multiples of (i + 1).

Our work presents an OPL that is a function of the distance between the tapers of the MZFI and uses (2). We propose an interferometer whose length is of the order of centimetres and facilitates manipulations to obtain the traditional and the harmonic OVE. The work presented the first-order harmonic OVE in three devices with the possibility of obtaining a second-order, even third-order harmonic OVE. Theoretically, the sensitivity would improve with the second and third harmonic orders, but it is necessary to conduct experimental tests to demonstrate it. To do so, it is essential to adequately choose distances between tapers of L_{Ref} that allow an increase for multiples of "i + 1" times the distance between tapers for L_{Sen}.

V. CONCLUSION

In summary, the generation of harmonic OVE was experimentally demonstrated using cascading sections of tapered single-mode fibres. The experimental results showed that the sensitivity (−3.9 to −33.3 nm/mm) and the M-factor (4.10–8.51) increased significantly compared with traditional OVE and single MZFI. Additionally, we observed that the distance between the tapers of the MZFI sensor exhibited an inversely proportional with sensitivity and directly proportional with the M-factor. Our configuration increases the sensitivity of a traditional interferometric micro-displacement sensor, making its manufacture more precise and flexible for specific applications. In addition, the proposed structure is reproducible, including the inner envelopes for the OVE harmonic, which facilitates spectral tracking owing to displacement and favors its analysis. Finally, the structure is simple, robust, and low-cost, making it suitable for several applications.

ACKNOWLEDGMENT

The authors would like to thank CONAHCYT(MX). LGR thanks CONAHCYT for the MSc scholarship. The authors also thank M.C. Jimenez-Mares for her valuable assistance tapering optical fibers.

REFERENCES

[1] A. D. Gomes, H. Bartelt, and O. Frazão, "Optical Vernier effect: Recent advances and developments," *Laser Photon. Rev.*, vol. 15, no. 7, pp. 1–16, 2021, doi: 10.1002/lpor.202000588.
[2] Y. Liu, X. Li, Y. nan Zhang, and Y. Zhao, "Fiber-optic sensors based on Vernier effect," *J. Int. Meas. Confederation*, vol. 167, 2021, Art. no. 108451, doi: 10.1016/j.measurement.2020.108451.
[3] M. Quan, J. Tian, and Y. Yao, "Ultra-high sensitivity Fabry–Perot interferometer gas refractive index fiber sensor based on photonic crystal fiber and Vernier effect," *Opt. Lett.*, vol. 40, no. 21, 2015, Art. no. 4891, doi: 10.1364/ol.40.004891.
[4] P. Chen, Y. Dai, D. Zhang, W. Xiaoyan, and M. Yang, "Cascaded-cavity Fabry-Perot interferometric gas pressure sensor based on Vernier effect," *Sensors*, vol. 18, 2018.
[5] Y. Li, C. Zhao, B. Xu, D. Wang, and M. Yang, "Optical cascaded Fabry–Perot interferometer hydrogen sensor based on Vernier effect," *Opt. Commun.*, vol. 414, pp. 166–171, 2018, doi: 10.1016/j.optcom.2017.12.012.
[6] J. Tian, Z. Li, Y. Sun, and Y. Yao, "High-sensitivity fiber-optic strain sensor based on the Vernier effect and separated Fabry-Perot interferometers," *J. Lightw. Technol.*, vol. 37, no. 21, pp. 5609–5618, Nov. 2019, doi: 10.1109/JLT.2019.2936174.
[7] F. Li et al., "Plug-in label-free optical fiber DNA hybridization sensor based on C-type fiber Vernier effect," *Sensors Actuators B Chem.*, vol. 354, 2022, Art. no. 131212, doi: 10.1016/j.snb.2021.131212.
[8] Z. Li et al., "Highly-sensitive fiber-optic F-P salinity sensor based on Vernier effect," *Opt. Fiber Technol.*, vol. 74, 2022, Art. no. 103148, doi: 10.1016/j.yofte.2022.103148.
[9] A. D. Gomes et al., "Optical harmonic Vernier effect: A new tool for high performance interferometric fibre sensors," *Sensors*, vol. 19, no. 24, pp. 1–18, 2019, doi: 10.3390/s19245431.
[10] P. M. R. Robalinho, A. D. Gomes, and O. Frazao, "High enhancement strain sensor based on Vernier effect using 2-fiber loop mirrors," *IEEE Photon. Technol. Lett.*, vol. 32, no. 18, pp. 1139–1142, Sep. 2020, doi: 10.1109/LPT.2020.3014695.

[11] A. D. Gomes et al., "Hollow microsphere combined with optical harmonic Vernier effect for strain and temperature discrimination," *Opt. Laser Technol.*, vol. 127, 2020, Art. no. 106198, doi: 10.1016/j.optlastec.2020.106198.

[12] A. D. Gomes et al., "Giant refractometric sensitivity by combining extreme optical Vernier effect and modal interference," *Sci. Rep.*, vol. 10, no. 1, pp. 1–14, 2020, doi: 10.1038/s41598-020-76324-7.

[13] P. Robalinho and O. Frazao, "Nano-displacement measurement using an optical drop-shaped structure," *IEEE Photon. Technol. Lett.*, vol. 33, no. 2, pp. 65–68, Jan. 2021, doi: 10.1109/LPT.2020.3044118.

[14] X. Yang et al., "Simplified highly-sensitive gas pressure sensor based on harmonic Vernier effect," *Opt. Laser Technol.*, vol. 140, 2021, Art. no. 107007, doi: 10.1016/j.optlastec.2021.107007.

[15] S. Wang et al., "In-situ adjustable fiber-optic piezometer based on parallelly structured external Fabry-Perot interferometers with Vernier effect and its harmonics," *Opt. Exp.*, vol. 29, no. 26, 2021, Art. no. 42800, doi: 10.1364/oe.445192.

[16] S. Liu, G. Lu, D. Lv, M. Chen, and Z. Zhang, "Sensitivity enhanced temperature sensor with cascaded Sagnac loops based on harmonic Vernier effect," *Opt. Fiber Technol.*, vol. 66, 2021, Art. no. 102654, doi: 10.1016/j.yofte.2021.102654.

[17] C. Zhou, Y. Song, Q. Zhou, J. Tian, and Y. Yao, "Ultra-high-sensitivity humidity fiber sensor based on harmonic Vernier effect in cascaded FPI," *Sensors*, vol. 22, no. 13, 2022, Art. no. 4816, doi: 10.3390/s22134816.

[18] C. Luo, X. Chen, and S. Wu, "Ultrasensitive fiber-based gas pressure sensor based on harmonic Vernier effect with enhanced contrast," *Opt. Laser Technol.*, vol. 156, 2022, Art. no. 108532, doi: 10.1016/j.optlastec.2022.108532.

[19] Z. Yang, W. YUAN, Z. Lian, and C. Yu, "Dual Fabry-Perot interferometers gas pressure sensor in parallel configuration based on hollow core Bragg fiber and harmonic Vernier effect," *Opt. Exp.*, vol. 30, no. 25, pp. 44420–44433, 2022, doi: 10.1364/oe.472475.

[20] L. Chen, J. Tian, Q. Wu, and Y. Yao, "Ultrahigh sensitivity temperature sensor based on harmonic Vernier effect," *IEEE Sensors J.*, vol. 23, no. 1, pp. 381–388, Jan. 2023, doi: 10.1109/JSEN.2022.3224719.

[21] L. Guillen-Ruiz, G. Anzueto-Sánchez, I. Torres-Gómez, J. Camas-Anzueto, A. Martínez-Rios, and G. Salceda-Delgado, "Experimental demonstration of optical Vernier effect by cascading tapered single-mode optical fibres," *Opt. Fiber Technol.*, vol. 70, 2022, Art. no. 102869, doi: 10.1016/j.yofte.2022.102869.

[22] A. R. D. C. Gomes, "Advanced fiber sensing technologies using microstructures and Vernier effect," Ph.D. dissertation, Univ. Porto, Porto, Portugal, 2021. [Online]. Available: https://repositorio-aberto.up.pt/bitstream/10216/133652/2/463400.pdf

[23] Y. Zhao, P. Wang, R. Lv, and X. Liu, "Highly sensitive airflow sensor based on Fabry-Perot interferometer and Vernier effect," *J. Lightw. Technol.*, vol. 34, no. 23, pp. 5351–5356, Dec. 2016, doi: 10.1109/JLT.2016.2615054.

[24] G. Zuo et al., "The order calibration of Vernier squared envelope extracted by the Hilbert-Huang transform," *J. Lightw. Technol.*, vol. 39, no. 6, pp. 1880–1886, Mar. 2021, doi: 10.1109/JLT.2020.3041625.

[25] N. E. Huang and S. S. P. Shen, *Hilbert-Huang Transform and its Applications*, vol. 16. Singapore: World Scientific, 2014.

[26] L. Xin, Z. Yang, J. Dou, Z. Liu, Z. Gao, and X. Zhang, "Hilbert transform-based envelope substitution method for non-uniform sampling signal correction in white-light interferometry," *Opt. Soc. Amer. Continuum*, vol. 3, no. 4, pp. 824–834, 2020, doi: 10.1364/osac.390435.